Backflow events under the effect of secondary flow of Prandtl's first kind

R. C. Chin,[1] R. Vinuesa,[2,3] R. Örlü,[2] J. I. Cardesa,[4] A. Noorani,[2,3]
M. S. Chong,[5] and P. Schlatter[2,3,*]

[1]*School of Mechanical Engineering, University of Adelaide, Adelaide, South Australia 5005, Australia*
[2]*SimEx/FLOW, Engineering Mechanics, KTH Royal Institute of Technology, SE-100 44 Stockholm, Sweden*
[3]*Swedish e-Science Research Centre (SeRC), SE-100 44 Stockholm, Sweden*
[4]*Institut de Mécanique des Fluides de Toulouse (IMFT), Université de Toulouse, 31400 Toulouse, France*
[5]*Department of Mechanical Engineering, University of Melbourne, Victoria 3010, Australia*

(Received 6 December 2019; accepted 8 July 2020; published 30 July 2020)

A study of the backflow events in the flow through a toroidal pipe at friction Reynolds number $Re_\tau \approx 650$ is performed and compared with the results in a straight turbulent pipe flow at $Re_\tau \approx 500$. The statistics and topological properties of the backflow events are analysed and discussed. Conditionally averaged flow fields in the vicinity of the backflow event are obtained, and the results for the torus show a similar streamwise wall-shear stress topology which varies considerably for the azimuthal wall-shear stress when compared to the pipe flow. In the region around the backflow events, critical points are observed. The comparison between the toroidal pipe and its straight counterpart also shows fewer backflow events and critical points in the torus. This is attributed to the secondary flow of Prandtl's first kind present in the toroidal pipe, which is responsible for the convection of momentum from the inner to the outer bend through the core of the pipe, and back from outer bend to the inner bend along the azimuthal direction. These results indicate that backflow events and critical points are genuine features of wall-bounded turbulence, and are not artefacts of specific boundary or inflow conditions in simulations and/or measurement uncertainties in experiments.

DOI: 10.1103/PhysRevFluids.5.074606

I. INTRODUCTION

A detailed assessment of the near-wall region in turbulent flows is a very complex problem, which involves a number of interesting fundamental questions including its modulation by the flow in the outer region [1–5]. The transport phenomena [6] present close to the wall, which can be characterized in terms of the wall-shear-stress vector field, are relevant to understand a wide range of applications, including cardiovascular flows [7] (e.g., in the context of Lagrangian wall-shear stress structures [8]) and heat transfer [9,10]. In particular, the presence of regions of instantaneous reverse flow (denoted in the present work as backflow events) in wall-bounded turbulence is a topic of relevance for the understanding of separation mechanisms, both in steady [11] and unsteady [12] aerodynamic applications. A recent review by Carlomagno and Ianiro [13] discussed that flow reversal produced by local pressure-gradient fluctuations in the near-wall region can initiate secondary vortices. It is reported that this flow reversal is one of two features (the other being vortex generation) that can enhance the heat-transfer characteristics in the flow. Moreover, backflow events and the topology of the wall-shear stress have been used to further understand the separation mechanisms from the perspective of dynamical systems [14], control theory [15], and reduced-order

*pschlatt@mech.kth.se

modeling [16], among others. Backflow events in turbulent channel flow were for the first time characterised in detail by Lenaers *et al.* [17], together with extreme wall-normal velocity fluctuations near the wall. In their direct numerical simulations (DNSs), they found that both the probability of finding a backflow event and the distance from the wall at which reverse flow was observed increased with Reynolds number. These indications show that there is a connection between the modulation of the near-wall region by the large-scale motions in the outer part of the flow and the presence of backflow events. This connection was quantitatively investigated by documenting the backflow event density beneath large-scale structures residing in the logarithmic layer. Their conclusions were confirmed in a DNS of turbulent channel flow [18] at a slightly higher Reynolds number, where a probability of finding backflow events of around 0.07% was reported at a friction Reynolds number of $\mathrm{Re}_\tau = 2000$. In both studies a strong connection between the presence of backflow events and energetic large-scale motions in the outer region were reported. These studies confirmed the indications in earlier works [19–21] regarding the presence of backflow events in wall-bounded turbulence, despite the fact that they had not been detected in certain measurement campaigns [22,23]. The more recent experimental study by Willert *et al.* [24], who performed particle image velocimetry (PIV) measurements in zero-pressure-gradient (ZPG) turbulent boundary layers (TBLs) at $\mathrm{Re}_\tau = 1000$ and 2700, confirmed the findings by Lenaers *et al.* [17] and Yao, Huang, and Xu [18]. Brücker [25] used micropillar sensors to measure the topology of the wall-shear stress vector in a ZPG TBL at $\mathrm{Re}_\tau \simeq 940$, and identified a probability of finding backflow events of around 0.05%, aligned with the results by Lenaers *et al.* [17] at approximately the same Re. Note that micro-pillar sensors, based on correlating the deflection of small flexible pillars on the wall and the shear stress, provide accurate measurements of the τ_w fluctuations (where τ_w is the wall-shear stress), as well as their spatial correlations [26–29]. Thus, Brücker [25] was able to determine that backflow events are correlated with strong spanwise gradients of the wall-shear stress, and characterised the topology of critical points (defined as points where both the wall-shear stress and the surface vorticity are zero). These backflow events are thought to strongly correlate with large-scale events in the logarithmic layer [17]. This correlation was further investigated using DNS of turbulent channel [30] and pipe [31] flows, and they reported that critical points are formed when large-scale motions transport vorticity toward the wall. Backflow events have also been studied in more complicated configurations, such as adverse-pressure-gradient (APG) TBLs, both numerically [32] and experimentally [33]. These studies show that APGs increase the probability of occurrence of backflow events, while their topology in inner-units remains unchanged.

While all of the aforementioned experimental studies investigating backflow events are able to document and characterise backflow events qualitatively and quantitatively, they often have difficulties to assess the Reynolds-number scaling of these extreme events, due to insufficient temporal and spatial resolution with increasing Reynolds number. However, the DNS studies discussed above are able to provide such resolution requirements. Given the fact that the existence of backflow events has been established beyond doubt in canonical wall-bounded flows, in this study we aim at evaluating the effect of a nonzero cross-stream velocity distribution (i.e., secondary flow) on such backflow events. The flow through curved pipes is characterised by a strong in-plane secondary flow of Prandtl's first kind driven by the centrifugal force and accompanied by a pressure gradient, which has a strong impact on the kinematics and dynamics of the flow [34,35]. This makes the toroidal pipe a very interesting flow case regarding backflow events. The relevance of this flow case is related to the fact that it serves as the common asymptotic limit of two distinct classes of important flow cases, i.e., the flow in spatially developing pipe bends (when entry effects become negligible), and the flow in helical pipes (when the torsion becomes negligible). Additionally, it serves as a test case with natural periodicity, which is experimentally difficult to realize, but not impossible as shown by Kühnen *et al.* [36]. This type of flow has recently been explored by means of DNS in terms of its stability [37] as well as laminar [38] and turbulent [39] base flows (covering a wide range of curvatures) and is here for the first time explored to study back-flow events.

In the present study we analyze the characteristics of back-flow events in toroidal pipes using a numerical approach similar to the one reported by Noorani and Schlatter [40]. The results are

also compared to the corresponding straight pipe at a similar Re_τ. In incompressible wall-bounded flows, the near-wall vorticity fields, which are related to the wall-shear stress, are associated with turbulence transport mechanisms [41]. Therefore, in this work we aim at further understanding such mechanisms in toroidal pipes by providing detailed analyses of the wall-shear stress distributions in this flow case.

II. METHOD

A. Pipe flow simulations

The turbulent pipe flow data used for the present study comes from a direct numerical simulation (DNS) [41,42]. The numerical scheme employed to perform the pipe flow simulations is detailed in Blackburn and Sherwin [43]. The scheme uses a spectral element discretization in the meridional semi-plane with an 11th-order Gauss–Lobatto–Legendre nodal-based expansion in each element and a Fourier discretization in the azimuthal direction. The details of the present simulation are summarised in Table I. The coordinate system is defined as x, $y = R_p - r$ (where R_p is the pipe radius and r is the radial distance measured from the pipe center) and $z = r\theta$, which are the streamwise, wall-normal, and azimuthal directions, respectively. The mesh resolutions in the streamwise and spanwise (azimuthal) directions are denoted by Δ_x and $\Delta_z = \Delta_{r\theta}$, respectively, and the corresponding lengths of the computational domain are L_x and L_z. The streamwise computational domain length is $L_x = 8\pi\delta$. The effects of insufficient computational length are well documented [44] (e.g., lack of convergence of higher-order turbulence statistics). The superscript "+" is used to denote viscous scaling, i.e., in terms of the friction velocity u_τ or the viscous length ν/u_τ.

B. Simulation of the flow through a toroidal pipe

The DNS of the turbulent flow through a toroidal pipe was performed using the numerical code Nek5000, developed at the Argonne National Laboratory [45] and based on spectral-element method (SEM) [46]. Lagrange interpolants of order N are used to expand the velocity and pressure, respectively, at the Gauss–Lobatto–Legendre (GLL) quadrature points within the spectral elements. The nonlinear terms in the incompressible Navier–Stokes equations are treated explicitly through third-order extrapolation (EXT3), and an implicit third-order backward differentiation (BDF3) scheme is used for the viscous terms. Numerical stability of the SEM was ensured through explicit filtering of 5% of the energy of the highest mode (see the work by Fischer and Mullen [47] for additional details). The simulations were carried out on the Cray XC40 system "Beskow," located at the PDC Center from KTH, running on 4096 cores.

The toroidal pipe under consideration is shown in Fig. 1, which is similar to the bent pipes considered by Noorani, El Khoury, and Schlatter [39]. Figure 1(a) shows the instantaneous streamwise wall-shear stress and in Fig. 1(b) a cross-sectional view of the torus is presented. The coordinate system for the torus is defined as $x = r_t\phi$ (where r_t denotes the radial distance with respect to the torus center), $y = R_p - r$ and $z = r\theta$, which are the streamwise, wall-normal and azimuthal directions, respectively. This is chosen to be consistent with the pipe flow notation. The corresponding instantaneous streamwise, wall-normal and azimuthal velocities are U, V and W. We consider a bulk Reynolds number $\mathrm{Re}_b = 2U_bR_p/\nu$ (based on bulk velocity U_b and pipe diameter $2R_p$) of 19 000, which yields a corresponding $\mathrm{Re}_\tau = 550$ in straight pipes [48]. As will

TABLE I. Computational parameters for the toroidal pipe and the pipe.

Flow case	Re_τ	L_x^+	L_z^+	Δ_x^+	Δ_z^+	Δ_y^+	N_x	N_y	N_z	$N_y \times N_z$	u_τ
Pipe	500	12566	3142	6.8	8.2	0.07	1940	160	384	–	5.88×10^{-2}
Torus	650	13614	4084	[3.62, 11.81]	[1.71, 5.61]	0.5	1936	–	–	189696	6.84×10^{-2}

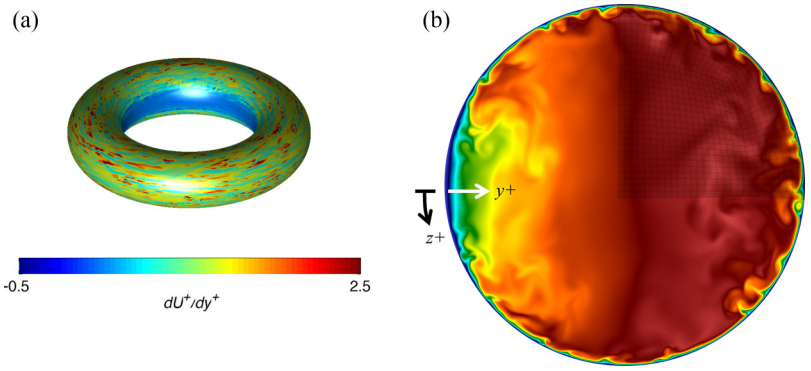

FIG. 1. (a) Instantaneous inner-scaled streamwise wall-shear stress in the torus. (b) Cross-sectional view of an instantaneous streamwise velocity field, also showing one quarter of the in-plane spectral-element mesh. Note that the individual GLL points within elements are also shown, and that in this panel dark blue and dark red correspond to -0.1 and 1.4, respectively. The coordinate system is defined as x, y and z, which are the streamwise (into the page), wall-normal, and azimuthal directions, respectively.

be discussed below, due to the presence of the secondary flow induced by the pipe curvature, the value of Re_τ depends on the particular azimuthal location, and the averaged value is different from 550. The friction Reynolds number based on the averaged u_τ is $\mathrm{Re}_\tau \approx 650$. Note that the Reynolds numbers are slightly different between the torus and pipe as shown in Table I. The geometry is completely defined with the curvature $\kappa = R_p/R_t$ (where R_t denotes the radius of the torus, i.e., the distance from the torus center to the pipe centreline), which in the present study is set to 0.3. The computational mesh is designed for a straight pipe first [39,48], following typical guidelines for DNS, and then this mesh is bent through analytical morphing to obtain the geometry of the toroidal pipe as discussed by Noorani, El Khoury, and Schlatter [39]. A total of 717 288 spectral elements with $N = 7$ was used to discretise the domain, which amounts to around 370 million grid points. The in-plane SEM mesh is shown in Fig. 1(b) and the simulation parameters are summarised in Table I. The simulations are run with constant mass flux, and periodicity is imposed in the streamwise direction. The laminar Poiseuille profile was used as initial condition, and low-amplitude pseudo-random noise was added to trigger transition to turbulence. After around 200 convective time units the turbulence could be considered fully developed and independent of the initial conditions. Thus, the data under consideration in the present work was obtained after the initial 200 time units of simulation. Note that although Nek5000 solves the Navier–Stokes equations in a Cartesian frame of reference, rotation matrices were employed to express all the tensors in the local toroidal frame of reference as stated previously.

In Fig. 2 we show a cross-sectional view of the mean velocity through the torus, so as to illustrate the effect of the secondary flow. First, it can be observed that the streamwise velocity exhibits very low speed at the inner bend, whereas the maximum is in the upper half of the cross section. The in-plane streamfunction Ψ shows the formation of the so-called Dean vortices, which are characteristic of the secondary flow of Prandtl's first kind present in bent pipes (see, e.g., Ref. [39]). The in-plane velocity magnitude shows a strong secondary flow along the azimuthal direction of the pipe, combined with milder convection of momentum directed from the inner to the outer bend of the pipe, as also indicated by the streamlines. The impact of these features on the near-wall events will be discussed in the remainder of the manuscript.

C. Definition of backflow events

Backflow events result from strong but spatially localized unsteady effects. The latter lead to brief lifetimes, as evidenced in studies of turbulent plane channels where regions of negative velocity and

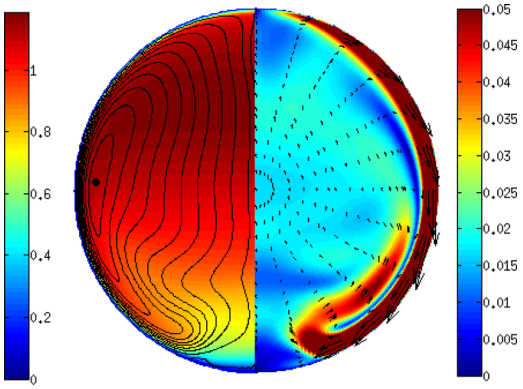

FIG. 2. (Left half) Pseudocolors of mean streamwise velocity with isocontours of the streamfunction Ψ; (right half) pseudocolors of mean in-plane velocity magnitude with a vector plot of the in-plane motion. Note that the maximum in-plane velocity magnitude is around 0.12 (very close to the wall), but the employed scale allows to better observe the details of the field.

critical points in the skin-friction fields were spatially time-tracked [30,49]. Other approaches to analyze unsteady separation are discussed by Surana *et al.* [50]. However, by means of instantaneous flow fields that are distant in time (compared to typical backflow object lifetimes), we can still collect valuable information such as average size and area density. That is one of the aims of the present study. The classification of backflow events is straightforward for the pipe flow, where negative dU/dy values correspond to backflow or reverse-flow events. This is not the case for the flow through a toroidal pipe as shown in Fig. 3. Figures 3(a) and 3(b) show the instantaneous streamwise wall-shear stress for the torus and pipe, respectively. It is clear that in the pipe flow, the streamwise wall-shear stress profile exhibits an homogeneous pattern in the spanwise direction, whereas in the torus the distribution varies significantly from the inner bend ($z/\delta = 0$ and 2π) to the outer bend ($z/\delta = \pi$) as shown in Noorani *et al.* [51]. Note that in the context of the present work the variable δ denotes both the pipe radius R_p in the torus and the pipe radius. In the straight pipe flow, without any external spanwise forcing, the mean spanwise wall-shear stress is zero. Note that the wall-shear stresses is directly proportional to the velocity gradient at the wall, i.e., $\tau_w \propto dU/dy|_{\text{wall}}$, therefore the velocity gradient is used as a reference for the wall-shear stress in this paper. In the toroidal pipe, the existence of secondary flow induces a nonzero spanwise wall-shear stress. The magnitude of the local spanwise wall-shear stress is highly dependent on the strength of the secondary flow and the azimuthal location. This local nonzero spanwise wall-shear stress and the local streamwise wall-shear stress result in a local preferential flow direction. Therefore, to determine the backflow events in a toroidal flow, the local mean wall-shear-stress angle has to be considered using the streamwise and spanwise wall velocity gradients $d\overline{U}/dy$ and $d\overline{W}/dy$, respectively. Consequently, negative events are defined when the flow direction is opposite to the local mean wall-shear-stress angle.

The probability density function of the orientation of the wall-shear-stress vector is shown, in the form of a wind-rose plot, for the torus and the pipe in Figs. 3(c), 3(e) and 3(d), 3(f), respectively. The wind rose plots essentially provide information of the magnitude and direction of the wall-shear-stress vector. Figure 3(d) shows that the wall-shear-stress vector in the pipe is oriented predominantly in the streamwise direction (denoted by $\pi/2$). However, in the flow through the toroidal pipe the wall-shear-stress vector exhibits three main preferential directions: the flow being aligned with the streamwise pressure gradient (denoted by $\pi/2$) and the flow at approximately $\pm 5\pi/18$ with respect to the streamwise pressure gradient direction. Comparing the zoomed-in wind-rose plots of the torus [Fig. 3(e)] and pipe [Fig. 3(f)] clearly shows that backflow events occur in both cases.

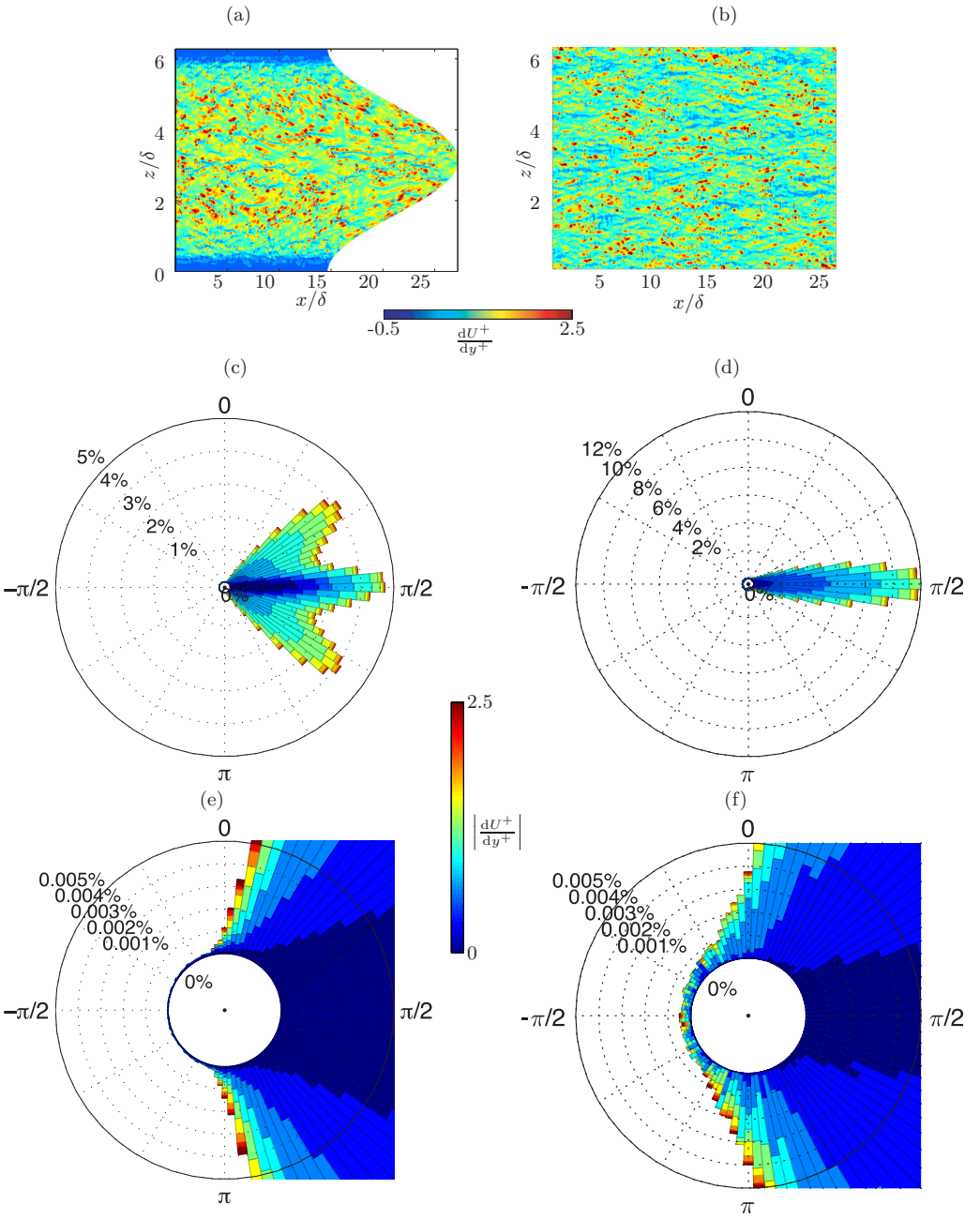

FIG. 3. Instantaneous streamwise wall-shear stress for (a) torus (unwrapped) and (b) pipe. Probability density function of the orientation of the wall-shear-stress vector and magnitude for (c) torus with (e) zoomed-in view and for (d) pipe with (f) zoomed-in view.

The results also show a higher percentage of backflow events in the pipe as compared to the torus. The temporal and streamwise average of the local wall-shear stress angle ψ (in degrees) is shown in Fig. 4(a), using the same angular frame of reference as the one considered in Fig. 3. The angle ψ at the inner and outer bends is $\psi = 90^\circ$, which implies that in these regions the wall-shear

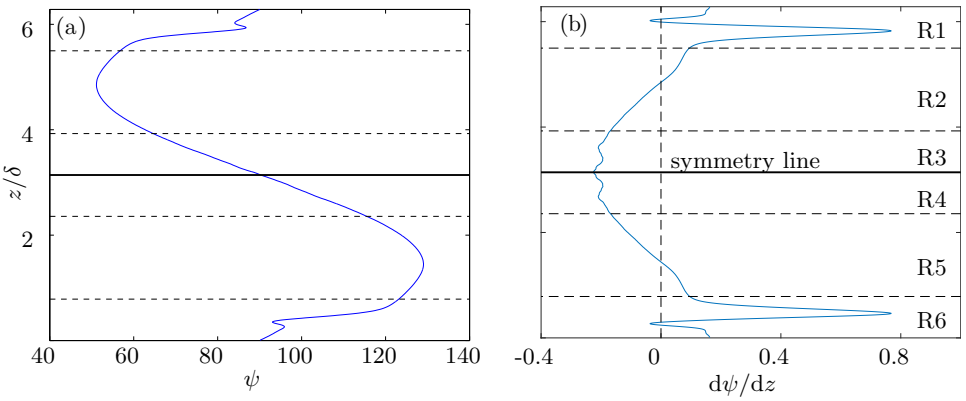

FIG. 4. (a) Local average wall-shear stress angle ψ (in degrees) for the torus. (b) Derivative of ψ in the azimuthal direction. The solid line denotes the location of the outer bend. The dash lines split the torus into six regions, denoted R1 to R6, used for analysis purposes.

stress vector is aligned with the streamwise direction, and that there is no preferential direction for the spanwise wall-shear stress. The angle ψ is continuously changing from the inner to the outer bend. As expected, our results clearly show that ψ is symmetrical about either the inner or the outer bend. Since, as observed in Fig. 3(c), there are three preferential directions of the wall-shear stress, we will split the toroidal wall surface into several different regions to account for the variation in the local flow direction.

To determine suitable regions to analyze backflow events, three distinct ψ values can be identified from Figs. 3(c) and 4(a), which are $\psi \approx 50^\circ$ (occurring at $z/\delta \approx 3\pi/2$), $\psi \approx 90^\circ$ (occurring at $z/\delta \approx 0$ and 2π) and $\psi \approx 130^\circ$ (occurring at $z/\delta \approx \pi/2$). In Fig. 3(c), the probability density function shows a range of angles of around $\pm 20^\circ$-25° from the three distinct ψ values $\psi = 50^\circ$, 90°, and 130°. A further analysis on the rate of change of ψ and $d\psi/dz$ is used to discriminate the regions as shown in Fig. 4(b). The torus wall surface is split into six regions, which are denoted from R1 to R6. Note that R1, R2, and R3 are mirrored regions of R6, R5, and R4, respectively. The regions R3 and R4 show an approximately constant $d\psi/dz$, R2 and R5 exhibit a constant slope of $d\psi/dz$ and the remaining R1 and R6 have steep variations in $d\psi/dz$.

Coincidentally, this is similar to splitting the wall surface into four quadrants (Q) along the circumference in the cross section. Each quadrant has an arc length of $L_{\text{arc}} = \pi/2$. The four quadrant are: $Q1 =$ R1$(0 < z/R_p < \pi/4)$ + R6 $(7/4\pi < z/R_p < 2\pi)$, $Q2 =$ R2 $(\pi/4 < z/R_p < 3/4\pi)$, $Q3 =$ R5 $(5/4\pi < z/R_p < 7/4\pi)$, and $Q4 =$ R3 $(3/4\pi < z/R_p < \pi)$ + R4 $(\pi < z/R_p < 5/4\pi)$.

III. RESULTS

The conditional average of the wall-shear stresses (or the velocity gradients), $d\mathbf{U}(x,z)/dy$ about a backflow event is computed as follows:

$$\left\langle \frac{d\mathbf{U}}{dy} \right\rangle = \left\langle \frac{d\mathbf{U}(x,z)}{dy} \middle| \arctan\left(\frac{dW(x,z)}{dy} \middle/ \frac{dU(x,z)}{dy} \right) \notin \left[\psi\left(\frac{z}{\delta}\right) - \frac{\pi}{2}, \psi\left(\frac{z}{\delta}\right) + \frac{\pi}{2} \right] \right\rangle. \quad (1)$$

The local wall-shear stress angle ψ_l is first evaluated using dW/dy and dU/dy, this angle ψ_l is then compared to the mean ψ (see Fig. 4) at the same z/δ location. If ψ_l is not within $\psi(z/\delta) \pm \pi/2$, it is considered a backflow event and will be included in the conditional average. $\langle d\mathbf{U}/dy \rangle = \langle d\mathbf{U}/dy \rangle(\Delta x, \Delta z)$, where the conditional average domain plane is bounded by $-100 \leqslant \Delta x \leqslant 500$, $-50 \leqslant \Delta z \leqslant 50$, with a backflow event nominally centered at (0,0). The conditional averaging of $\langle dU^+/dy^+ \rangle$ and $\langle dW^+/dy^+ \rangle$ in the vicinity of a backflow event is first performed for the entire toroidal pipe without considering the local flow angle. The results are compared with

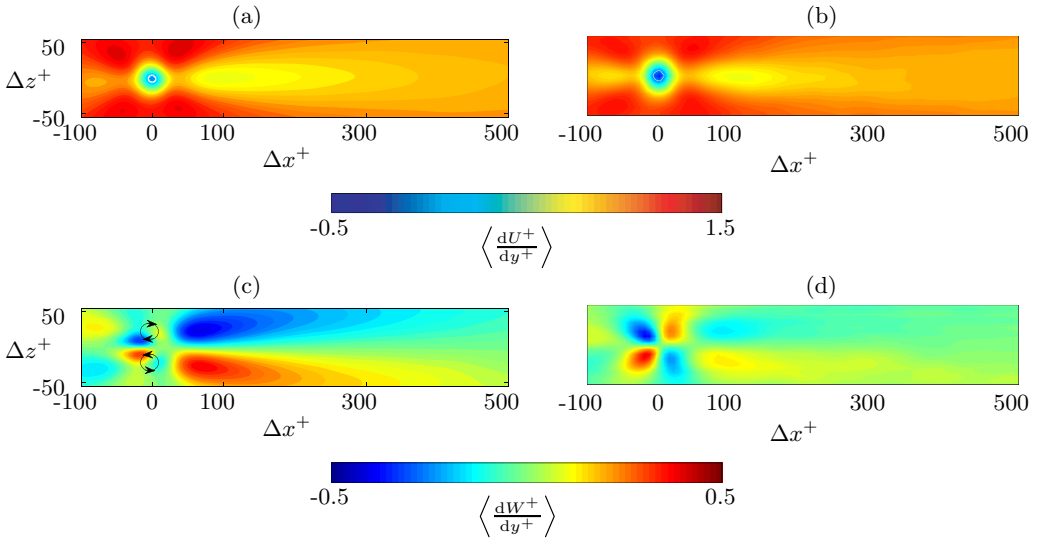

FIG. 5. Distributions of $\langle dU^+/dy^+ \rangle$ (a), (b) and $\langle dW^+/dy^+ \rangle$ (c), (d) conditionally averaged to the presence of a backflow event at $\Delta x = \Delta y = 0$. The evaluation was performed over the entire azimuthal direction of the toroidal pipe. Left panels correspond to the torus and right panels to the pipe. The white contour in panels (a) and (b) denote zero streamwise wall-shear stress.

the pipe flow and are shown in Fig. 5. The top row, i.e., Figs. 5(a) and 5(b), show a comparison of the streamwise wall-shear stress $\langle dU^+/dy^+ \rangle$ in the torus and in the pipe. Note that in these figures the center of the backflow event is located at $\Delta x = \Delta z = 0$. The overall distribution is qualitatively similar in both cases, with low $\langle dU^+/dy^+ \rangle$ values right upstream and right downstream of the backflow event. The backflow events are flanked by regions of strong $\langle dU^+/dy^+ \rangle$ values, and interestingly the torus exhibits consistently larger shear-stress values in the vicinity of the backflow event than the pipe. The mean diameter of these backflow events differs between the torus and the pipe, with a mean diameter of about 16 viscous units in the torus and around 20 viscous units in the pipe. Note that a diameter of around 20 viscous units was also reported in the adverse-pressure-gradient turbulent boundary layer developing on the suction side of a wing section [32] and in channel-flow simulations [17].

Figures 5(c) and 5(d) show the spanwise wall-shear-stress distribution $\langle dW^+/dy^+ \rangle$ for the torus and the pipe, respectively. In the case of the torus, the backflow event is flanked by two regions of positive (negative) $\langle dW^+/dy^+ \rangle$, immediately followed by small areas of opposite sign in the downstream direction. This pattern suggests the presence of a pair of counter-rotating vortices in the vicinity of the backflow events, as illustrated in Fig. 5(c), which is kinematically consistent with the presence of a region of reverse streamwise velocity. The symmetry of these vortices is to be interpreted with care, since instantaneously only one vortex could be present and indeed Lenaers *et al.* [17] show single oblique vortical structures in instantaneous visualisations above backflow regions. In the region around the backflow event, i.e., $\Delta x^+ \approx [-50, 20]$, $\Delta z^+ \approx [-25, 25]$, this alternating pattern in $\langle dW^+/dy^+ \rangle$ is also present in the pipe, although its topology is slightly different: the regions of positive (negative) spanwise wall-shear stress flanking the backflow event are larger, as opposed to what is observed in the torus. It is interesting to note that at farther downstream distance ($\Delta x^+ > 50$) of the backflow event in the toroidal pipe, the $\langle dW^+/dy^+ \rangle$ signature is significantly stronger and longer than the upstream distribution, whereas the opposite is observed in the pipe.

Since the results in Fig. 5 for the torus are a combination of contributions from the different regions defined in Fig. 4(b) (R1 to R6), it will be natural to investigate the influence of the

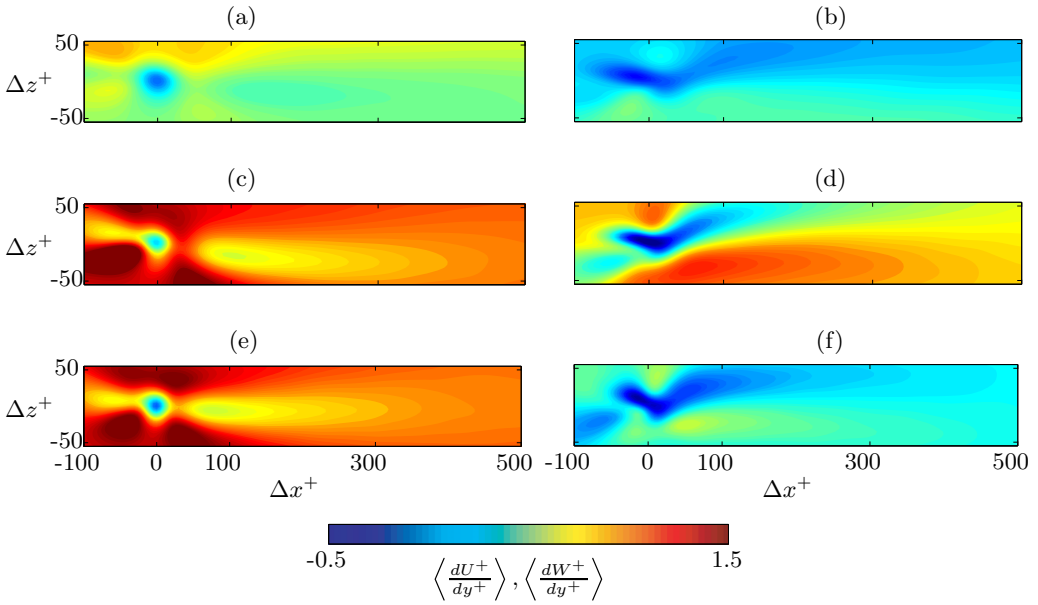

FIG. 6. (Left panels) streamwise wall-shear stress $\langle dU^+/dy^+ \rangle$ and (right panels) spanwise wall-shear stress $\langle dW^+/dy^+ \rangle$. The results are shown for (a), (b) region R1, (c), (d) region R2, and (e), (f) region R3. Regions are as defined in Fig. 4(b).

secondary motion in the flow within the various areas of the torus. Due to the fact that the regions are symmetrical about the symmetry line (see Fig. 4), only results from regions R1, R2, and R3 will be presented, which, however, include the contributions from their symmetrical counterparts to increase the sample space. The streamwise wall-shear stress $\langle dU^+/dy^+ \rangle$ from the torus is shown in Figs. 6(a), 6(c), and 6(e) for regions R1, R2, and R3, respectively. This field exhibits significant differences in R1 compared to the field obtained when the contributions from all the regions are combined, as can be observed comparing Figs. 6(a) and 5(a). As documented in the literature [39,52–54], the pipe curvature induces an in-plane secondary flow which convects momentum from the inner to the outer bend through the core of the pipe, and from the outer bend back to the inner bend along the azimuthal direction, as shown in Fig. 1(c). This secondary flow amounts to around 15% of the bulk velocity for the present curvature, which implies that it has a strong effect on the local flow features. The conditionally averaged field in R1 shows a significantly weaker shear-stress field at the inner bend, with a small region of higher $\langle dU^+/dy^+ \rangle$ on one of the sides of the backflow event, induced by the secondary flow returning to the inner bend along the pipe wall. This reduced wall-shear stress was also observed by Noorani, El Khoury, and Schlatter [39] in bent pipes with high curvature, together with a plateau in τ_w and reduced turbulent kinetic energy at the inner bend, which suggest partial relaminarization of the flow in this region. The distribution shown in Fig. 6(e) for region R3, i.e., for the outer bend, resembles the one in Fig. 5(a), although the latter exhibits smaller shear-stress values due to the fact that it also accounts for the weaker field present in the inner bend. Regarding region R2, the $\langle dU^+/dy^+ \rangle$ field shown in Fig. 6(c) shares some similarities with the outer bend, although its asymmetry is produced by the strong effect of the secondary flow in that region of the pipe. Figures 6(b), 6(d), and 6(f) show the spanwise wall-shear stress $\langle dW^+/dy^+ \rangle$ for regions R1, R2, and R3, respectively. Here the profiles are clearly different from the ones obtained by considering the whole torus, which are shown in Fig. 5(c). This discrepancy is somewhat expected, since the secondary flow imprints a strong spanwise velocity *footprint* on the flow. The distributions for regions R1, R2, and R3 show a clear spanwise inclination, which is most prominent in Fig. 6(d), corresponding to region R2. Regions R1 and R3, i.e., the inner and

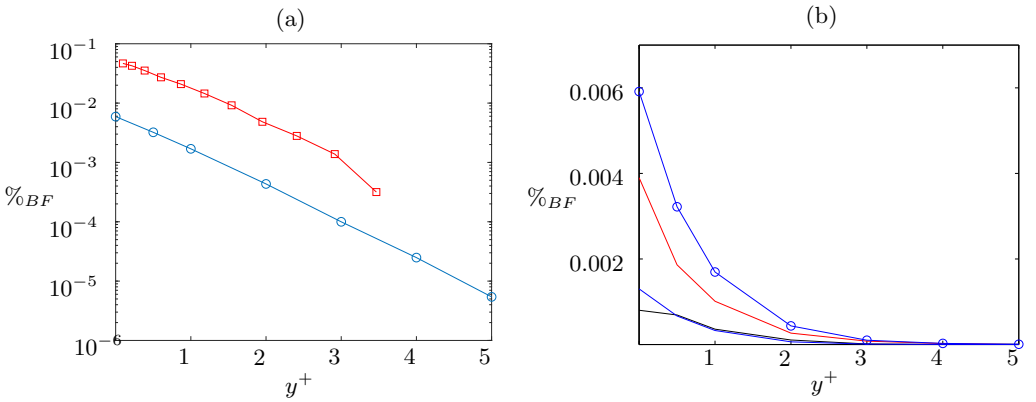

FIG. 7. (a) Percentage of backflow events $\%_{\mathrm{BF}}$ with increasing inner-scaled wall-normal distance for torus (blue line with ○) and pipe [red line with (box)]. (b) Backflow events $\%_{\mathrm{BF}}$ for torus decomposed into different regions. R1 + R6 blue line; R2 + R5 red line; and R3 + R4 black line. Note that the percentages for the regions are given such that their sum equates to the total percentage of backflow events. The blue line with dots is the same torus data as in panel (a).

outer bend regions, are therefore slightly less influenced by the spanwise motion imposed by the secondary flow.

Next, a comparison of the percentage of backflow events ($\%_{\mathrm{BF}}$) with increasing wall-normal distance y^+ is performed for the toroidal pipe and the pipe flow and is shown in Fig. 7. The percentage of backflow events decreases exponentially with increasing wall-normal distance, an observation in agreement with previously reported results [17,32]. Regarding the results from the torus, Fig. 7(a) shows that the percentage of backflow events is almost an order of magnitude lower than that of the pipe flow at a comparable Reynolds number. Moreover, the $\%_{\mathrm{BF}}$ trend shows a similar exponential decay with y^+. A decomposition of the $\%_{\mathrm{BF}}$ for the torus into the different regions defined in Fig. 4 is shown in Fig. 7(b), and also in Fig. 8. The regions R1 + R6 and R3 + R4, which are least subjected to the influence of the secondary flow, have very similar $\%_{\mathrm{BF}}$ away from

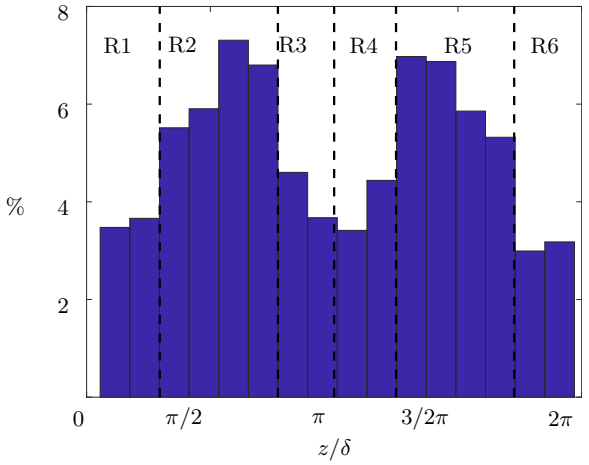

FIG. 8. Histogram of backflow events in the toroidal pipe along the spanwise direction. R1 to R6 are the different regions as defined in Fig. 4. The histogram is scaled to 100% of the total 0.006% occurrence of backflow events at the wall; cf. Table II.

TABLE II. Summary of backflow statistics in toroidal pipe and pipe flow. Note that the average of the percentage area of backflow events for the sum of the different regions of the toroidal pipe equates to the total percentage and number (indicated in boldface), respectively.

Quantity	Torus	Pipe
Percentage area of backflow	**0.006**%	**0.05**%
Percentage area of backflow for R1+R6	0.0010%	–
Percentage area of backflow for R2+R5	0.0038%	–
Percentage area of backflow for R3+R4	0.0012%	–
Number of backflow events (per 10^6 viscous unit area)	**0.3**	**1.8**
Mean diameter of backflow event (in viscous units)	**16**	**18**
Number of critical points (per 10^6 viscous unit area)	**0.35**	**2**

the wall. The $\%_{\mathrm{BF}}$ for region $\mathrm{R2}+\mathrm{R5}$ is, however, consistently larger than in the other regions, such that approximately $2/3$ of the backflow events are encountered in this region, i.e., in $1/3$ of the area. These results suggest that the strong spanwise secondary motion is less effective in reducing the occurrence of backflow events (with respect to the straight pipe) in regions $\mathrm{R2}+\mathrm{R5}$, while the formation of backflow events is even more significantly reduced in regions $\mathrm{R1}+\mathrm{R6}$ and $\mathrm{R3}+\mathrm{R4}$. It can be stated that the vortical structures required for the production of backflow events are significantly affected by the secondary flow in the toroidal pipe. Further inspection of Figs. 5(c) and 5(d) indicates that the spanwise wall-shear stress pattern responsible for the pair of counter-rotating vortices is weaker in the torus, a fact that is connected with the lower occurrence of reverse flow events. As reported by Vinuesa, Örlü, and Schlatter [32], APG TBLs exhibit higher occurrence of backflow events than ZPGs at the same Reynolds number. This is due to the fact that the wall-normal convection produced by the APG reduces the near-wall velocity, thus promoting the formation of regions of negative velocity. In the case under study here, the strong secondary flow convects momentum from the inner to the outer bend of the pipe; therefore, the flow on the outer bend experiences a strong convection toward the wall, with the opposite effect to that of an APG, thus resulting in a reduction of backflow events. As reported by Lenaers *et al.* [17], backflow events are absent in laminar flows, and are only produced as extreme events in turbulent flows. As discussed above, the strong convection away from the inner bend produces laminarlike conditions, as can be observed for instance in Fig. 1(b), therefore justifying the reduction of backflow events in this region. Overall, the present results indicate that the percentage of backflow events drops to around zero for wall-normal locations above $y^+ = 5$. It is interesting to observe that critical points, which exist in the vicinity of these backflow events [31,49,55], occur in similar numbers to backflow events for a given flow. Therefore, less critical points in the torus than in the pipe is reported.

A summary of the statistics for the backflow events in the toroidal and the straight pipes is presented in Table II. The toroidal pipe consistently shows a lower occurrence of backflow events (both in terms of percentage area of the wall and number of events per 10^6 viscous unit area) when compared to the pipe flow. The further decomposition of the torus statistics ($\%_{\mathrm{BF}}$ at the wall) into the three main regions are also shown in Table II. Our results clearly indicate that the secondary flow present in regions R2 and R5 is less effective in reducing the appearance of backflow events (with respect to the straight pipe) compared with that in the other four regions.

IV. CONCLUSIONS

A DNS of the turbulent flow through a toroidal pipe at $\mathrm{Re}_\tau \simeq 650$ was performed, using the spectral-element code Nek5000 [45], with the aim of analyzing the characteristics of the wall-shear stress vector. Backflow events, i.e., regions of reverse flow, were characterised in the torus and compared with the ones obtained in a DNS of turbulent pipe flow at $\mathrm{Re}_\tau \simeq 500$. Our results show that backflow events are less numerous in the toroidal pipe than in the pipe, with probabilities of

occurrence of approximately 0.006% and 0.05% in both cases, respectively. The fields of streamwise and spanwise wall-shear stress conditioned to the presence of a backflow event are stronger in the torus, and the diameter of the reverse flow regions is smaller than in the pipe. The diameter is around 16 viscous units in the former, while its value is about 18 in the pipe, in agreement with the results reported in other channel flow simulations [17] and in APG TBLs [32]. Note that, although the two flows are compared at different Reynolds numbers, the Re effect is much weaker than the discrepancy observed in the two cases, as reported by Ref. [17]. These differences are therefore explained by the effect of the secondary flow present in the torus, which convects momentum from the inner to the outer bend through the core of the pipe, and back from the outer to the inner bend through the pipe walls. This secondary flow, which amounts to around 15% of the bulk velocity [39] for the present curvature, inhibits the formation of backflow events in the outer bend through a mechanism opposite to the one reported in APG TBLs [32]. However, the significant wall-normal convection from the inner bend produces laminar-like conditions, which also lead to a dramatic reduction in the emergence of reverse-flow regions [17]. It is important to note that although it is common to impose periodicity in the streamwise and spanwise directions in turbulent pipe flow simulations, in the torus the flow is naturally streamwise-periodic. Therefore, the present results provide clear evidence that backflow events are genuine features and not artifacts of specific boundary or inflow conditions in simulations and/or measurement uncertainties in experiments. Future extensions of the present study will utilize the entire flow field of the toroidal pipe to investigate flow structures above these backflow events and critical points, which occur in close vicinity.

ACKNOWLEDGMENTS

This work was supported with supercomputing resources provided by the Phoenix HPC service at the University of Adelaide. In addition, computer time was provided by the Swedish National Infrastructure for Computing (SNIC). This study was funded in part by the Coturb Grant (Grant No. ERC-2014.AdG-669505) of the European Research Council. R.C.C. acknowledges the financial support of the Australian Research Council. R.V., R.Ö., and P.S. acknowledge the funding provided by the Swedish Research Council (VR) and the Knut and Alice Wallenberg Foundation.

[1] R. Mathis, N. Hutchins, and I. Marusic, Large-scale amplitude modulation of the small-scale structures in turbulent boundary layers, J. Fluid Mech. **628**, 311 (2009).

[2] P. Schlatter and R. Örlü, Quantifying the interaction between large and small scales in wall-bounded turbulent flows: A note of caution, Phys. Fluids **22**, 051704 (2010).

[3] I. Marusic, R. Mathis, and N. Hutchins, Predictive model for wall-bounded turbulent flow, Science **329**, 193 (2010).

[4] R. Vinuesa, M. H. Hites, C. E. Wark, and H. M. Nagib, Documentation of the role of large-scale structures in the bursting process in turbulent boundary layers, Phys. Fluids **27**, 105107 (2015).

[5] E. Dogan, R. Örlü, D. Gatti, R. Vinuesa, and P. Schlatter, Quantification of amplitude modulation in wall-bounded turbulence, Fluid Dyn. Res. **51**, 011408 (2019).

[6] J. Klewicki, C. Chin, H. M. Blackburn, A. Ooi, and I. Marusic, Emergence of the four layer dynamical regime in turbulent pipe flow, Phys. Fluids **24**, 045107 (2012).

[7] E. K. Poon, U. Hayat, V. Thondapu, A. Ooi, M. Asrar Ul Haq, S. Moore, N. Foin, S. Tu, C. Chin, J. P. Monty, I. Marusic, and P. Barlis, Coron. Artery Dis. **26**, e43 (2015).

[8] A. Arzani, A. M. Gambaruto, G. Chen, and S. C. Shadden, Lagrangian wall shear stress structures and near-wall transport in high-Schmidt-number aneurysmal flows, J. Fluid Mech. **790**, 158 (2016).

[9] T. Dairay, V. Fortuneé, E. Lamballais, and L. E. Brizzi, Direct numerical simulation of a turbulent jet impinging on a heated wall, J. Fluid Mech. **764**, 362 (2015).

[10] Z. Wu, D. Laurence, H. Iacovides, and I. Afgan, Direct simulation of conjugate heat transfer of jet in channel crossflow, Int. J. Heat Mass Transf. **110**, 193 (2017).
[11] R. Vinuesa, S. M. Hosseini, A. Hanifi, D. S. Henningson, and P. Schlatter, Pressure-gradient turbulent boundary layers developing around a wing section, Flow Turbul. Combust. **99**, 613 (2017).
[12] P. S. Negi, R. Vinuesa, P. Schlatter, A. Hanifi, and D. S. Henningson, Unsteady aerodynamic effects in pitching airfoils studied through large-eddy simulations, in *Proceedings of the 10th International Symposium on Turbulence and Shear Flow Phenomena (TSFP-10)* (2017).
[13] G. Carlomagno and A. Ianiro, Thermo-fluid-dynamics of submerged jets impinging at short nozzle-to-plate distance: A review, Exp. Therm. Fluid Sci. **58**, 15 (2014).
[14] A. Surana, O. Grunberg, and G. Haller, Exact theory of three-dimensional flow separation. Part 1. Steady separation, J. Fluid Mech. **564**, 57 (2006).
[15] M.-R. Alam, W. Liu, and G. Haller, Closed-loop separation control: An analytic approach, Phys. Fluids **18**, 043601 (2006).
[16] S. L. Brunton, C. W. Rowley, and D. R. Williams, Reduced-order unsteady aerodynamic models at low Reynolds numbers, J. Fluid Mech. **724**, 203 (2013).
[17] P. Lenaers, Q. Li, G. Brethouwer, P. Schlatter, and R. Örlü, Rare backflow and extreme wall-normal velocity fluctuations in near-wall turbulence, Phys. Fluids **24**, 035110 (2012).
[18] Y. C. Yao, W. X. Huang, and C. X. Xu, Amplitude modulation and extreme events in turbulent channel flow, Acta Mech. Sin. **34**, 1 (2018).
[19] G. Johansson, An experimental study of the structure of a flat plate turbulent boundary layer, using laser-Doppler velocimetry, Ph.D. dissertation, Chalmers University of Technology, Göteborg (Sweden), 1988.
[20] P. R. Spalart and G. N. Coleman, Numerical study of a separation bubble with heat transfer, Eur. J. Mech. B/Fluids **16**, 169 (1997).
[21] Z. W. Hu, C. L. Morfey, and N. D. Sandham, Wall pressure and shear stress spectra from direct simulations of channel flow, AIAA J. **44**, 1541 (2006).
[22] H. Eckelmann, The structure of the viscous sublayer and the adjacent wall region in a turbulent channel flow, J. Fluid Mech. **65**, 439 (1974).
[23] K. J. Colella and W. L. Keith, Measurements and scaling of wall shear stress fluctuations, Exp. Fluids **34**, 253 (2003).
[24] C. Willert, C. Cuvier, J. Foucaut, J. Klinner, M. Stanislas, J. Laval, S. Srinath, J. Soria, O. Amili, C. Atkinson, S. S. C.J. Kähler and, R. Hain, A. Schröder, R. Geisler, J. Agocs, and A. Röse, Experimental evidence of near-wall reverse flow events in a zero pressure gradient turbulent boundary layer, Exp Therm Fluid Sci **91**, 320 (2018).
[25] C. Brücker, Evidence of rare backflow and skin-friction critical points in near-wall turbulence using micropillar imaging, Phys. Fluids **27**, 031705 (2015).
[26] C. Brücker, D. Bauer, and H. Chaves, Dynamic response of micro-pillar sensors measuring fluctuating wall-shear-stress, Exp. Fluids **42**, 737 (2007).
[27] S. Große and W. Schröder, Mean wall-shear stress measurements using the micro-pillar shear-stress sensor MPS3, Meas. Sci. Technol. **19**, 015403 (2008).
[28] R. Vinuesa and R. Örlü, Measurement of wall-shear stress, in *Experimental Aerodynamics*, edited by S. Discetti and A. Ianiro (CRC Press, Boca Raton, FL, 2017).
[29] Y. Liu, M. Klaas, and W. Schröder, Measurements of the wall-shear stress distribution in turbulent channel flow using the micro-pillar shear stress sensor MPS3, Exp. Thermal Fluid Sci. **106**, 171 (2019).
[30] J. I. Cardesa, J. P. Monty, J. Soria, and M. S. Chong, The structure and dynamics of backflow in turbulent channels, J. Fluid Mech. **880**, R3 (2019).
[31] R. C. Chin, J. P. Monty, M. S. Chong, and I. Marusic, Conditionally averaged flow topology about a critical point pair in the skin friction field of pipe flows using direct numerical simulations, Phys. Rev. Fluids **3**, 114607 (2018).
[32] R. Vinuesa, R. Örlü, and P. Schlatter, Characterization of backflow events over a wing section, J. Turbul. **18**, 170 (2017).

[33] M. Bross, T. Fuchs, and C. J. Kähler, Interaction of coherent flow structures in adverse pressure gradient turbulent boundary layers, J. Fluid Mech. **873**, 287 (2019).
[34] A. Kalpakli Vester, R. Örlü, and P. H. Alfredsson, Turbulent flows in curved pipes: Recent advances in experiments and simulations, Appl. Mech. Rev. **68**, 050802 (2016).
[35] Z. Wang, R. Örlü, P. Schlatter, and Y. M. Chung, Direct numerical simulation of a turbulent 90° bend pipe flow, Int. J. Heat Fluid Flow **73**, 199 (2018).
[36] J. Kühnen, M. Holzner, B. Hof, and H. Kuhlmann, Experimental investigation of transitional flow in a toroidal pipe, J. Fluid Mech. **738**, 463 (2014).
[37] J. Canton, P. Schlatter, and R. Örlü, Modal instability of the flow in a toroidal pipe, J. Fluid Mech. **792**, 894 (2016).
[38] J. Canton, R. Örlü, and P. Schlatter, Characterization of the steady, laminar incompressible flow in toroidal pipes covering the entire curvature range, Int. J. Heat Fluid Flow **66**, 95 (2017).
[39] A. Noorani, G. K. El Khoury, and P. Schlatter, Evolution of turbulence characteristics from straight to curved pipes, Int. J. Heat Fluid Flow **41**, 16 (2013).
[40] A. Noorani and P. Schlatter, Swirl-switching phenomenon in turbulent flow through toroidal pipes, Int. J. Heat Fluid Flow **61**, 108 (2016).
[41] C. Chin, J. Philip, J. Klewicki, A. Ooi, and I. Marusic, Reynolds-number-dependent turbulent inertia and onset of log region in pipe flows, J. Fluid Mech. **757**, 747 (2014).
[42] C. Chin, J. P. Monty, and A. Ooi, Reynolds number effects in DNS of pipe flow and comparison with channels and boundary layers, Int. J. Heat Fluid Flow **45**, 33 (2014).
[43] H. M. Blackburn and S. J. Sherwin, Formulation of a Galerkin spectral element-fourier method for three-dimensional incompressible flows in cylindrical geometries, J. Comput. Phys. **197**, 759 (2004).
[44] C. Chin, A. S. H. Ooi, I. Marusic, and H. M. Blackburn, The influence of pipe length on turbulence statistics computed from direct numerical simulation data, Phys. Fluids **22**, 115107 (2010).
[45] P. F. Fischer, J. W. Lottes, and S. G. Kerkemeier.
[46] M. O. Deville, P. F. Fischer, and E. H. Mund, *High-order Methods for Incompressible Fluid Flow* (Cambridge University Press, Cambridge, UK, 2002).
[47] P. Fischer and J. Mullen, Filter-based stabilization of spectral element methods, C. R. Acad. Sci. Paris **332**, 265 (2001).
[48] G. El Khoury, P. Schlatter, A. Noorani, P. Fischer, G. Brethouwer, and A. Johansson, Direct numerical simulation of turbulent pipe flow at moderately high Reynolds numbers, Flow Turbul. Combust. **91**, 475 (2013).
[49] J. I. Cardesa, J. P. Monty, J. Soria, and M. S. Chong, Skin-friction critical points in wall-bounded flows, J. Phys.: Conf. Ser. **506**, 012009 (2014).
[50] A. Surana, G. B. Jacobs, O. Grunberg, and G. Haller, An exact theory of three-dimensional fixed separation in unsteady flows, Phys. Fluids **20**, 107101 (2008).
[51] A. Noorani, G. Sardina, L. Brandt, and P. Schlatter, Particle transport in turbulent curved pipe flow, J. Fluid Mech. **793**, 248 (2016).
[52] H. Ito, Friction factors for turbulent flow in curved pipes, J. Basic Eng. **81**, 123 (1959).
[53] S. A. Berger, L. Talbot, and L.-S. Yao, Flow in curved pipes, Annu. Rev. Fluid Mech. **15**, 461 (1983).
[54] P. Bradshaw, Turbulent secondary flows, Annu. Rev. Fluid Mech. **19**, 53 (1987).
[55] M. S. Chong, J. P. Monty, C. Chin, and I. Marusic, The topology of skin friction and surface vorticity fields in wall-bounded flows, J. Turbul. **13**, N6 (2012).